A Velocity *k*-Space Analysis of Flow Effects in Echo-Planar and Spiral Imaging

Dwight G. Nishimura, Pablo Irarrazabal, Craig H. Meyer

A velocity *k*-space formalism facilitates the analysis of flow effects for imaging sequences involving time-varying gradients such as echo-planar and spiral. For each sequence, the velocity *k*-space trajectory can be represented by $k_v(k_r)$; that is, its velocity-frequency (k_v) position as a function of spatial-frequency (k_r) position. In an echo-planar sequence, k_v is discontinuous and asymmetric. However, in a spiral sequence, k_v is smoothly varying, circularly symmetric, and small near the k_r origin. To compare the effects of these trajectory differences, simulated images were generated by computing the *k*-space values for an in-plane vessel with parabolic flow. Whereas the resulting echo-planar images demonstrate distortions and ghosting that depend on the vessel orientation, the spiral images exhibit minimal artifacts.

Key words: flow imaging; fast imaging; angiography; magnetic resonance imaging.

INTRODUCTION

Fast-scan sequences such as echo-planar and spiral are being increasingly applied to flow-imaging situations, particularly in regions where respiration poses a problem (1–3). Because these sequences involve relatively long readouts in the presence of time-varying gradients, their ability to image flowing material accurately is of concern. Previous work by Duerk and Simonetti (4), Butts and Riederer (5), and Irarrazabal and Nishimura (6) have examined this issue, focusing primarily on the response to a moving spin.

In this paper, we invoke a velocity *k*-space formalism (7, 8) to gain insights into the flow effects of echo-planar and spiral sequences. This formalism also facilitates the computer simulation of flow images to compare these fast-scan sequences (9). We choose to emphasize the *k*-space interpretation because such interpretations have proven invaluable in the analysis of MR (both readout and excitation), especially when time-varying gradients are involved.

In the ensuing sections, we review velocity *k*-space, derive a relevant vessel model, and examine the *k*-space trajectories of the different sequences. We then present simulated flow images generated via this Fourier-based framework.

MRM 33:549–556 (1995)

From the Department of Electrical Engineering, Stanford University, Stanford, California.

Address correspondence to: Dwight G. Nishimura, Durand 345, Information Systems Laboratory, Stanford University, Stanford, CA 94305.

Received July 12, 1994; revised December 5, 1994; accepted December 19, 1994.

This work was supported by NSF BCS 9058556, NIH HL 39297, NIH NS 29434, NIH CA 50948, and GE Medical Systems.

P.I. is on leave from the Department of Electrical Engineering, Universidad Catolica de Chile.

0740-3194/95 $3.00

THEORY

Including the effects of constant-velocity flow, the MR baseband signal equation can be written as

$$s(t) = \int_{\mathbf{r}}\int_{\mathbf{v}} m(\mathbf{r},\mathbf{v}) e^{-i2\pi(\mathbf{k}_r(t)\cdot\mathbf{r}+\mathbf{k}_v(t)\cdot\mathbf{v})}\, d\mathbf{r}d\mathbf{v}, \quad [1]$$

where the spatial and velocity parameters are

$$r = [x\ y\ z],$$
$$v = [u\ v\ w], \quad [2]$$

and the *k*-space parameters are

$$\mathbf{k}_r(t) = \frac{\gamma}{2\pi}\int_0^t \mathbf{G}(\tau)\, d\tau,$$
$$\mathbf{k}_v(t) = \frac{\gamma}{2\pi}\int_0^t \tau\mathbf{G}(\tau)\, d\tau, \quad [3]$$

We use *u*, *v*, and *w* to denote velocity in the *x*, *y*, and *z* directions, respectively. In this signal equation, $m(\mathbf{r}, \mathbf{v})$ corresponds to the state of the magnetization at $t = 0$.

Upon inspection, Eq. [1] can be rewritten as

$$s(t) = M(\mathbf{k}_r(t),\mathbf{k}_v(t)), \quad [4]$$

where $M(\mathbf{k}_r, \mathbf{k}_v)$ is the six-dimensional (6D) Fourier transform of $m(\mathbf{r}, \mathbf{v})$. Therefore, s(t) provides values of the Fourier transform of $m(\mathbf{r}, \mathbf{v})$ along some trajectory in 6D Fourier space that depends on the zeroth and first moments of the applied gradient waveforms. These signal values (and hence the values of $M(\mathbf{k}_r, \mathbf{k}_v)$) map to the raw data function $I(\mathbf{k}_r)$, which is typically a function of only the spatial-frequency variables. The resulting image $i(\mathbf{r})$ is simply the inverse Fourier transform of $I(\mathbf{k}_r)$. Flow effects thus depend on the particular mapping of $M(\mathbf{k}_r, \mathbf{k}_v)$ values to $I(\mathbf{k}_r)$. Ideally, to avoid flow effects, $I(\mathbf{k}_r) = M(\mathbf{k}_r, 0)$; that is, the sequence is "flow-compensated" ($\mathbf{k}_v = 0$) at each spatial-frequency position. Unfortunately this condition is usually impractical to achieve.

In this paper, we restrict the analysis to 2D imaging of in-plane flow (in the *xy* plane) because the effects of constant through-plane flow are independent of the 2D imaging sequence. Therefore, simulation of the received signal $s(t)$ (and raw data function $I(k_x, k_y)$) requires specification of both the object $m(x, y, u, v)$ and the *k*-space trajectory $(k_x(t),k_y(t),k_u(t),k_v(t))$. In the following sections,

we elaborate on (1) the object model and (2) the *k*-space trajectories for the echo-planar and spiral sequences.

Object Model

We first consider a simple illustrative situation where an object $m_s(x, y)$ (at $t = 0$) moves at a constant speed with velocity components (u_o, v_o). In this case,

$$m(x,y,u,v) = m_s(x,y)\delta(u - u_o, v - v_o). \quad [5]$$

An example relevant to flow imaging is a horizontal vessel of infinite extent and of circular cross section (radius R), as shown in Fig. 1. If this vessel is entirely contained in the image plane, then

$$m(x,y,u,v) = 2(R^2 - y^2)^{1/2}\delta(u - u_o, v) \qquad |y| < R. \quad [6]$$

This expression corresponds to a plug-flow condition in which the velocity in the x direction is u_o. The term $2(R^2 - y^2)^{1/2}$ gives the projection through a circular cross section (integrating along the slice direction z and assuming unit density). Because the vessel is horizontal, Eq. [6] contains no x dependence.

The 4D Fourier transform of Eq. [6] is

$$M(k_x,k_y,k_u,k_v) = \delta(k_x)R\frac{J_1(2\pi Rk_y)}{k_y}e^{-i2\pi u_o k_u}. \quad [7]$$

The presence of plug flow gives rise to a linear phase term along the k_u axis. For $k_u = 0$ (or $u_o = 0$), Eq. [7] contains no flow dependence and reduces to the transform of a cylindrical object.

We can expand on this vessel model by considering parabolic flow with the same horizontal vessel geometry. With parabolic flow, the u-velocity component within the lumen depends on the (y, z) position and is given by

$$u = f(y,z) = u_m\left(1 - \frac{y^2 + z^2}{R^2}\right) \qquad y^2 + z^2 < R^2, \quad [8]$$

where u_m is the maximum velocity. To determine $m(x, y, u, v)$, we first note that the projection in the z direction now involves a range of velocities. Therefore, we require a velocity distribution function $p(u)$ along each chord of the circular lumen to express $m(x, y, u, v)$. For spins along a chord a distance y_o from the origin (Fig. 1), we calculate $p(u)$ given that the spatial magnetization is of unit density and that $u = f(y_o, z)$. We first note that the Jacobian of this transformation is df/dz and that two z positions along each chord map to a particular velocity u. Hence,

$$p(u) = \frac{2}{\left|\frac{df}{dz}\right|}. \quad [9]$$

Evaluating this equation for $z = f^{-1}(u) = ((1 - u/u_m)R^2 - y_o^2)^{1/2}$, we find that

$$p(u) = \frac{R^2}{u_m}\frac{1}{((1 - u/u_m)R^2 - y_o^2)^{1/2}}, \quad [10]$$

a function of y position since $p(u)$ pertains to a chord through the lumen. Had we considered the velocity distribution function for the entire lumen, a similar analysis would show that $p(u)$ is a uniform function from 0 to u_m, implying an average velocity of $u_m/2$. Finally, given Eq. [10] and considering a general y position, we arrive at

$$m(x,y,u,v) = \delta(v)\frac{R^2}{u_m}\frac{1}{((1 - u/u_m)R^2 - y^2)^{1/2}} \qquad 0 < u < u_m \qquad |y| < \left(\left(1 - \frac{u}{u_m}\right)R^2\right)^{1/2}. \quad [11]$$

Again, there is no x dependence in Eq. [11] because of the horizontal vessel orientation. Figure 2a depicts this distribution as a function of u and y. Compared to the case of plug flow, the spatial and velocity dependencies are no longer separable with parabolic flow.

We can write the 4D Fourier transform of $m(x, y, u, v)$ from Eq. 11 as

$$M(k_x,k_y,k_u,k_v) = \delta(k_x)\int_{u=0}^{u_m}\int_{y=-a}^{a}\frac{R^2}{u_m}\frac{1}{(a^2 - y^2)^{1/2}}e^{-i2\pi(k_y y + k_u u)}\,dy\,du, \quad [12]$$

where $a = ((1 - u/u_m)R^2)^{1/2}$. Using the 1D Fourier transform relationship:

$$\int_{-a}^{a}\frac{1}{(a^2 - y^2)^{1/2}}e^{-i2\pi k_y y}\,dy = \pi J_0(2\pi a k_y), \quad [13]$$

Eq. [12] reduces to

$$M(k_x,k_y,k_u,k_v) = \delta(k_x)\frac{\pi R^2}{u_m}\int_0^{u_m} J_0\left(2\pi k_y\sqrt{(1 - u/u_m)R^2}\right)e^{-i2\pi k_u u}\,du. \quad [14]$$

The remaining integral is difficult to evaluate analytically but may be computed for specific values of k_y and k_u. The result is shown in Fig. 2b which displays the magnitude of M in $k_u - k_y$ space. Again for $k_u = 0$, the function reduces to the transform of a cylinder.

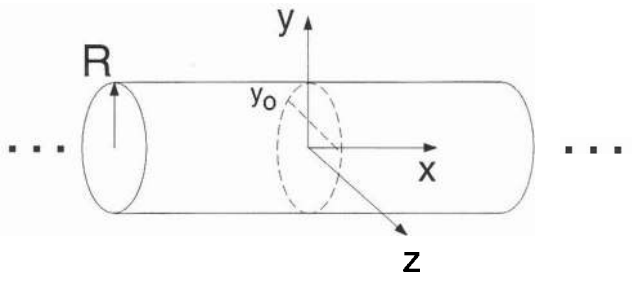

FIG. 1. Vessel model: a straight in-plane vessel of radius R with parabolic flow. If the image section (in xy) encompasses the entire vessel, then the velocity distribution must be evaluated along a chord parallel to z at each y position.

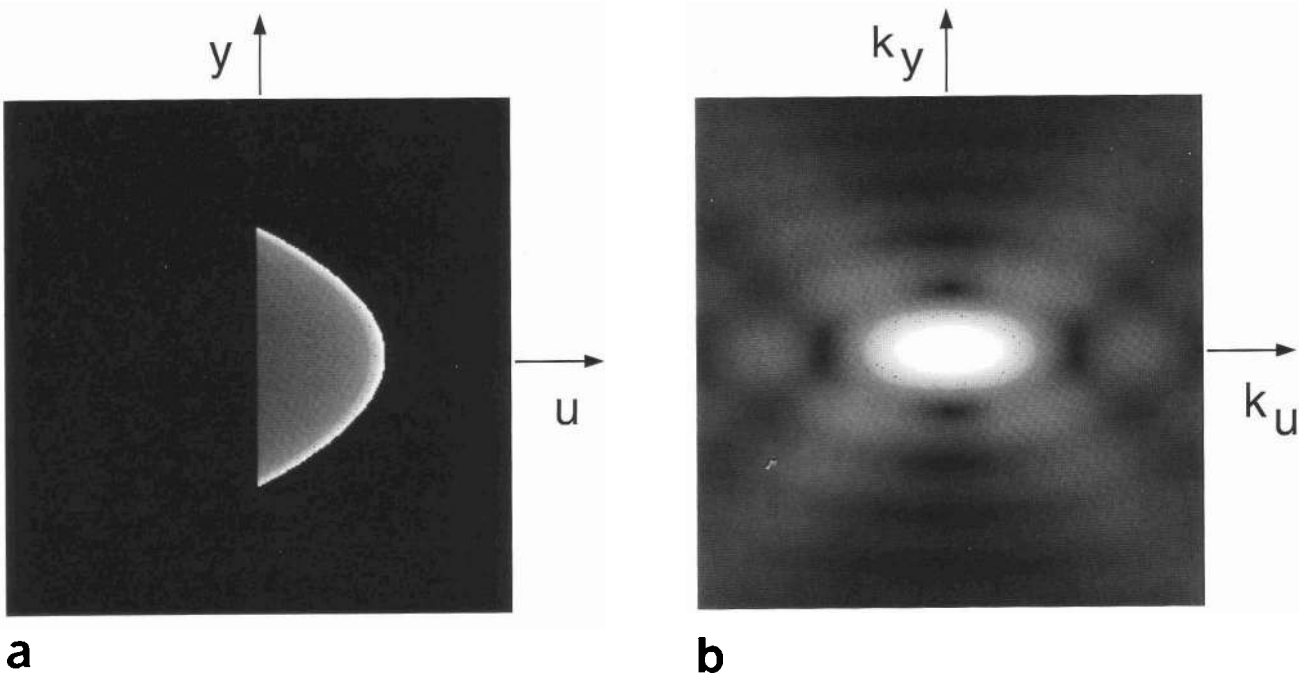

FIG. 2. $m(u, y)$ and $M(k_u, k_y)$: (a) magnetization function for parabolic flow through a vessel parallel to x. (b) 2D Fourier transform (magnitude) of (a).

k-Space Trajectories

We will consider idealized gradient-echo versions of blipped echo-planar and spiral sequences. In addition, we assume that both the echo-planar and spiral sequences are interleaved versions which fill *k*-space after multiple excitations. Their timing diagrams and corresponding spatial-frequency trajectories (for a single interleaf) are shown in Figs. 3 and 4, assuming a maximum gradient amplitude of 1 G/cm but infinitely fast rise times.

For echo-planar, the acquisition begins at the far corner of *k*-space and proceeds in a raster-like manner, blipping upwards in the k_y direction (Fig. 3b) to acquire 16 lines per excitation. The sequence is also assumed to be flow compensated in the blip direction (y) (10, 11); that is, k_v is set to zero when crossing the origin of *k*-space. To acquire the next interleaf in the echo-planar scan, the entire raster pattern in *k*-space is shifted in the k_y direction by a small increment. In addition, we assume a gradually time-shifted version of the gradients between interleaves (12, 13), which is important for smoothing the *k*-space trajectory as discussed later.

For spiral scanning, the acquisition begins at the *k*-space origin and spirals outward at a constant linear velocity (Fig. 4b) (2). To acquire the next interleaf in the spiral scan, the entire spiral trajectory is simply rotated by an incremental angle. Because each interleaf samples the *k*-space origin, the spiral sequence does not involve preparatory gradient lobes or time-shifting.

We assume a raw data matrix size of 256 × 256 with a maximum spatial-frequency extent of 5.1 cycles/cm, amounting to a spatial resolution of about 1 mm. The readout interval differs slightly between the two sequences: echo planar = 39.5 ms (ignoring the preparatory lobes); spiral = 32 ms. Another difference between the two is that the spiral sequence covers a circular region in

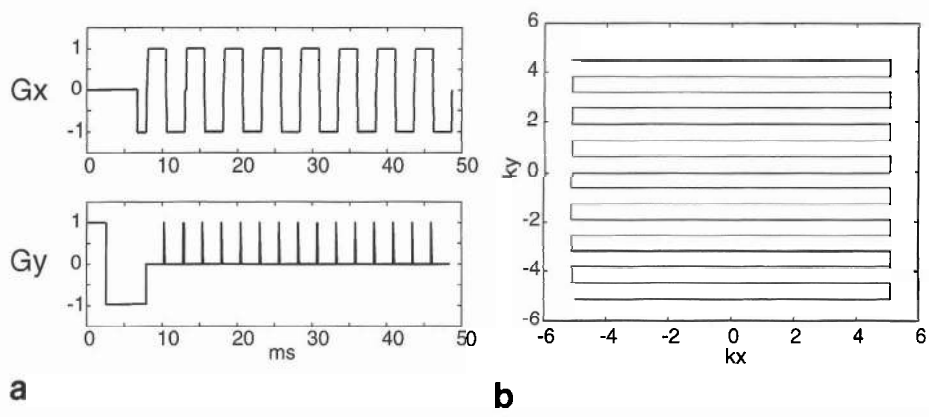

FIG. 3. Echo-planar sequence: timing diagram and $k_x k_y$ trajectory for a single interleaf.

k_xk_y space while the echo-planar sequence covers a square region.

One display of the velocity k-space trajectory depicts $k_u(k_x, k_y)$ and $(k_v(k_x, k_y))$ as gray levels in a 2D "image" of the spatial-frequency plane. Such depictions are presented in Figs. 5 and 6 for the echo planar and spiral sequences respectively (intermediate gray corresponds to zero amplitude). An alternative display is given in Fig. 7 which shows a portion of the central area of k_xk_y space. At each (k_x, k_y) position, the arrow represents the vector $[k_u\ k_v]$; hence both the amplitude and direction of the first moment are apparent.

For the echo-planar sequence (Figs. 5 and 7a), there exists discontinuities in the behavior of $[k_u\ k_v]$ due to the interleaving and the square-wave readout (G_x) gradient. For example, along the k_y axis, k_u is a square-wave function that jumps between some value k_{uo} and zero (Fig. 5a). This oscillation corresponds to G_x being flow compensated on alternate gradient echoes during the readout (an even-echo rephasing phenomenon). The behavior of k_v (Fig. 5b) is smooth due to the time-shifting of the interleaves that was mentioned earlier; without the time-shifting, k_v would also exhibit discontinuous behavior. For k_v, there exists both a linear and quadratic variation with k_y. The linear variation corresponds to material flowing along y being displaced in y by an amount dependent on the non-zero TE. From a k-space perspective, this displacement occurs because the linear variation in k_v with k_y position gives rise to linear phase in the raw data for constant-velocity material. For k_u, there exists mainly a linear variation with k_x but the slope of this variation increases from one readout line to the next. Given the train of readout lines after excitation, this steady increase in slope corresponds to increasing displacements in x because the readout lines occur at progressively later times.

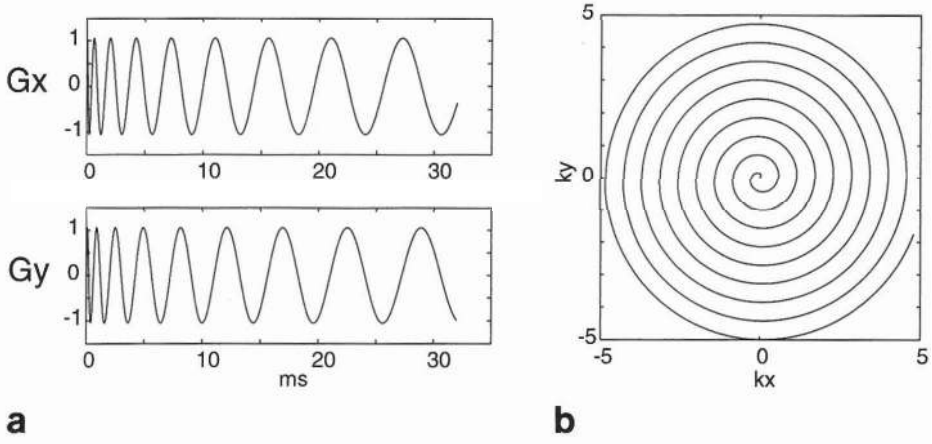

FIG. 4. Spiral sequence: timing diagram and k_xk_y trajectory for a single interleaf.

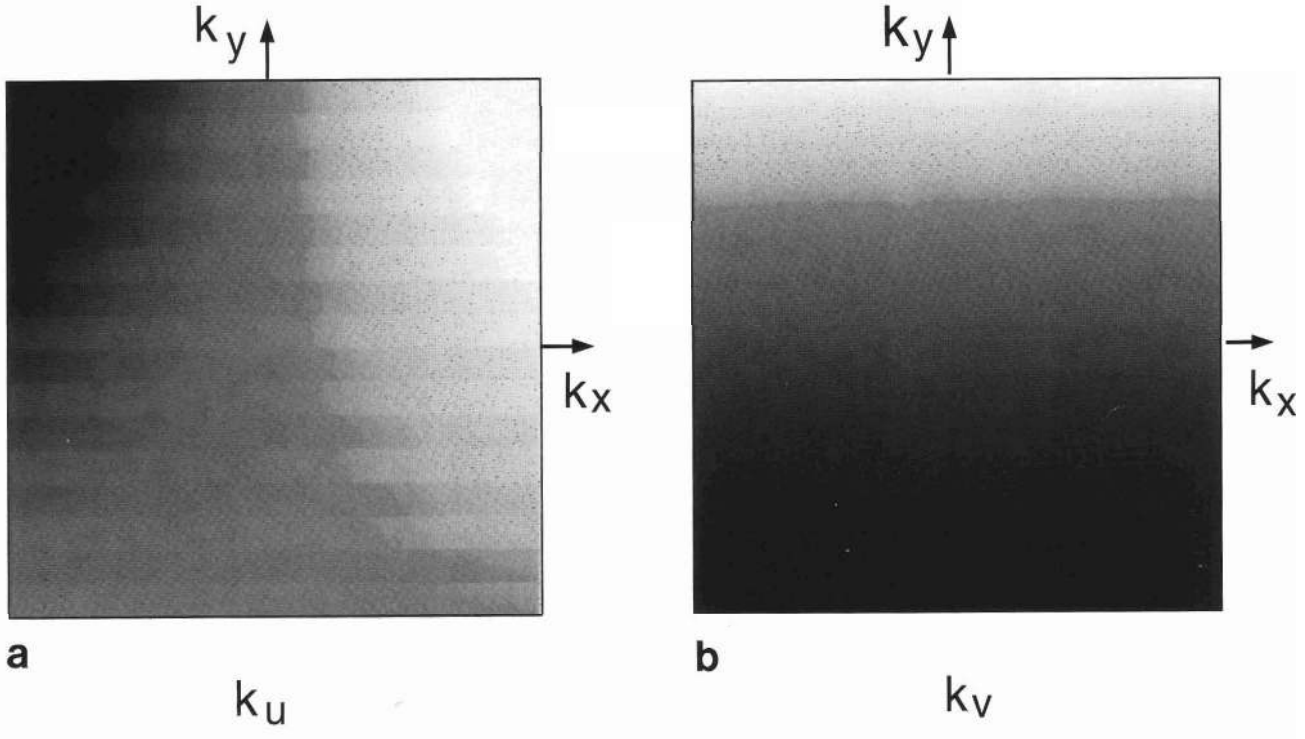

FIG. 5. Echo-planar velocity k-space trajectory: (a) $k_u(k_x, k_y)$, displayed as a gray level (neutral gray corresponds to zero). (b) $k_v(k_x, k_y)$.

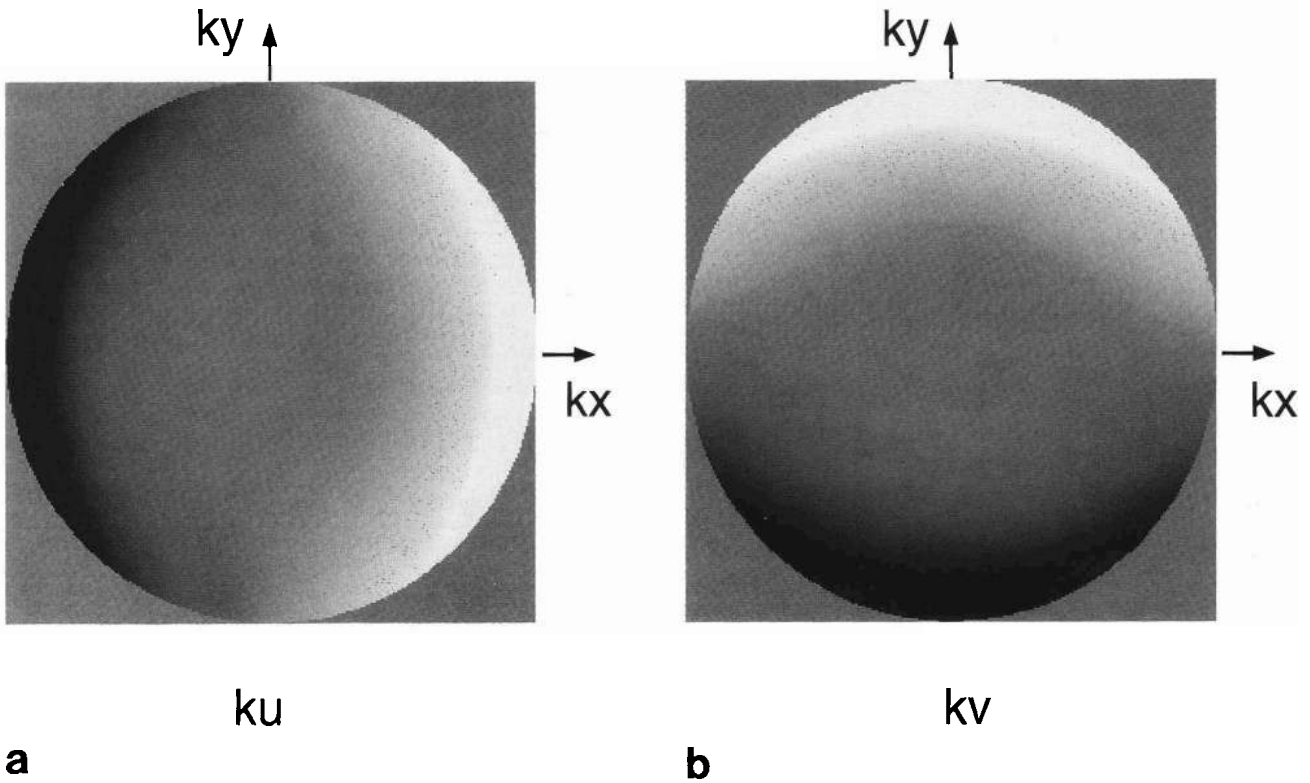

FIG. 6. Spiral velocity *k*-space trajectory: (a) $k_u(k_x, k_y)$, displayed as a gray level (neutral gray corresponds to zero). (b) $k_v(k_x, k_y)$.

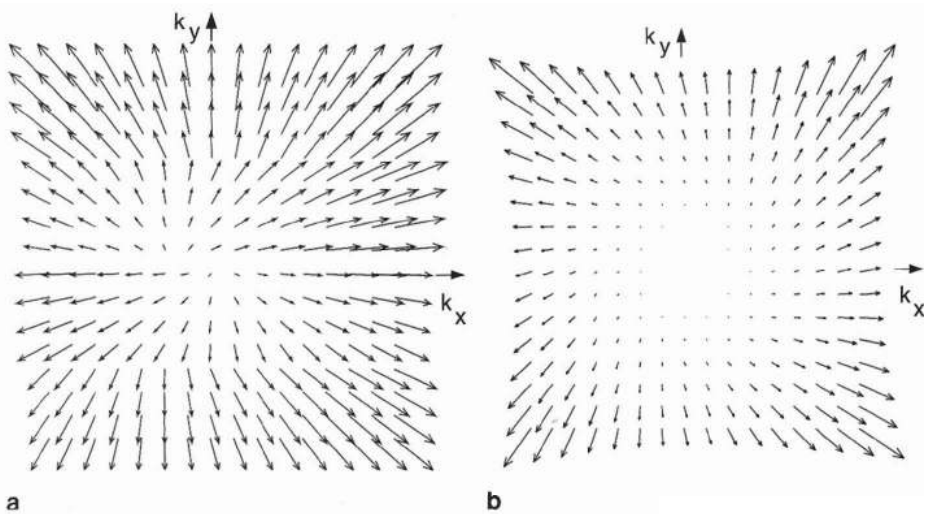

FIG. 7. Velocity *k*-space trajectories: (a) echo-planar-the vector $[k_u\ k_v]$ is displayed as a function of (k_x, k_y) position. The center portion of *k*-space is shown. (b) Spiral.

The spiral trajectory (Figs. 6 and 7b) exhibits significantly different behavior than the echo-planar trajectory. One salient property of the spiral trajectory is its circular symmetry (apparent in Fig. 7b). Also the length and direction of the vector $[k_u\ k_v]$ change smoothly, growing with radial distance from the origin, and largely pointing away from the origin.

SIMULATION RESULTS

Given an object model and a timing diagram for a given sequence, the general procedure to generate a flow image using the velocity *k*-space framework is summarized below.

1. Determine $M(k_x, k_y, k_u, k_v)$ for the object.
2. Compute $k_u^{seqn}(k_x,k_y)$ and $k_v^{seqn}(k_x,k_y)$ for the imaging sequence.
3. Let the raw data $I(k_x, k_y) = M(k_x,k_y,k_u^{seqn}(k_x,k_y),k_v^{seqn}(k_x,k_y))$.
4. Take the inverse Fourier transform of $I(k_x, k_y)$ to reconstruct the image $i(x, y)$.

For our simulations, we consider the k_u and k_v maps for echo-planar and spiral scanning as shown in Figs. 5 and 6, while for the object, we use the infinitely long in-plane vessel with a circular lumen and parabolic flow. Because the vessel is assumed to be of infinite extent, generation of the raw data is conveniently constrained to reside along a line in k_xk_y space. For the horizontal vessel, this line is along the k_y axis. Using the rotation property of Fourier transforms, we can rotate the $M(k_x,$

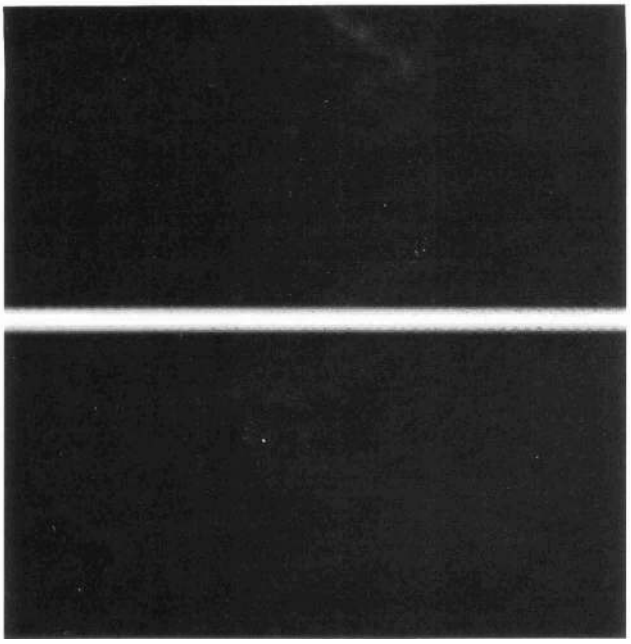

FIG. 8. Ideal vessel image for the simulations. 1-cm diameter vessel in an image FOV of 25.6 cm.

k_y, k_u, k_v) derived for a horizontal vessel to generate vessel images at any orientation in the xy plane. To isolate the effects of flow during the readout, this simulation neglects other notable considerations such as off-resonance and in-flow enhancement effects.

Figures 8–10 present the results of the simulations. The reference image (no flow) for a horizontal vessel of diameter 1 cm (in an image field-of-view of 25.6 cm) is given in Fig. 8. Figure 9 shows the simulated images for both the echo-planar and spiral sequence when the average flow velocity is 20 cm/s (maximum velocity of 40 cm/s). Figures 9a–9c are the echo-planar images for vessel orientations of 0°, 45°, and 90°. Because the response with spiral scanning is circularly symmetric, we show results for only the horizontal (0 degree) orientation (Fig. 9d). Repeating the simulations but at a higher average flow velocity of 40 cm/s, the corresponding echo-planar and spiral results are displayed in Fig. 10.

DISCUSSION

These simulations demonstrate substantially different flow-imaging performance between echo-planar and spiral. Apparent in the echo-planar images are intensity distortions and ghosting that depend on the vessel orientation, consistent with the analyses of Duerk and Simonetti (4), Butts and Riederer (5), and Simonetti *et al.* (14). The results with the spiral sequence clearly demonstrate excellent immunity to flow artifacts. In fact, simulations with average velocities over 2 m/s continued to reveal minimal artifacts in the spiral images.

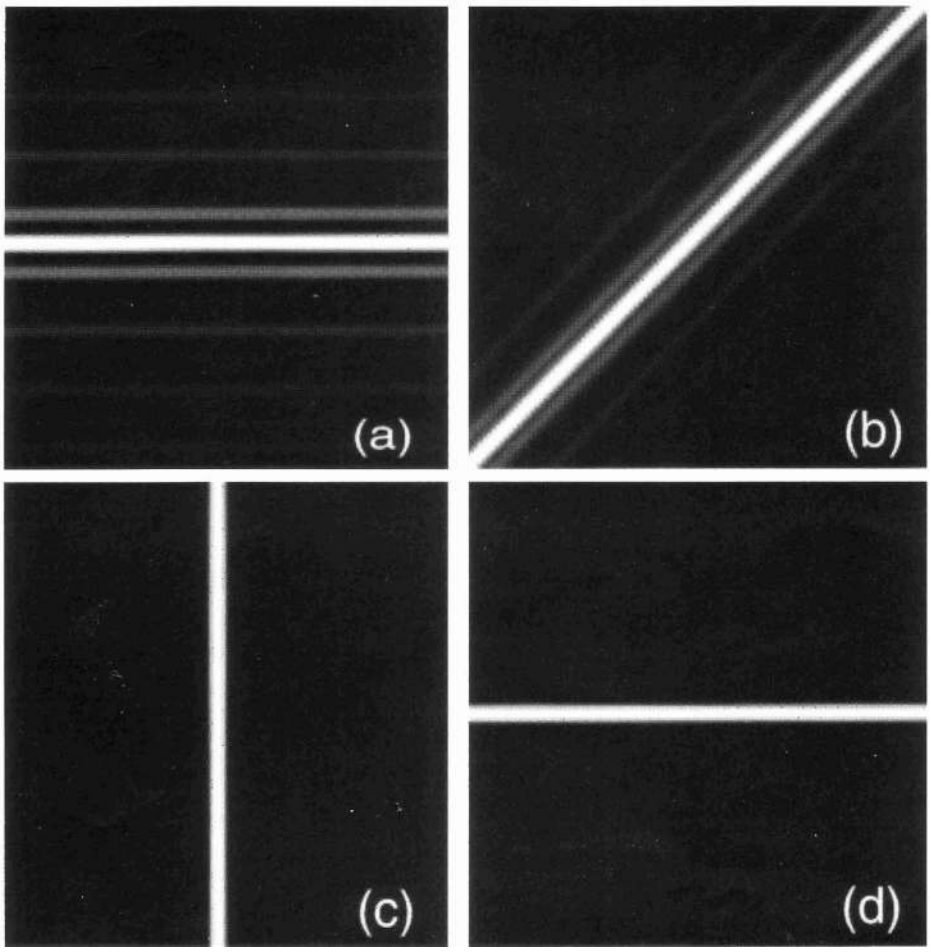

FIG. 9. Simulated echo-planar and spiral images: average velocity of 20 cm/s. (a)–(c) Echo-planar images for horizontal, diagonal, and vertical vessel orientations, respectively. (d) Spiral image.

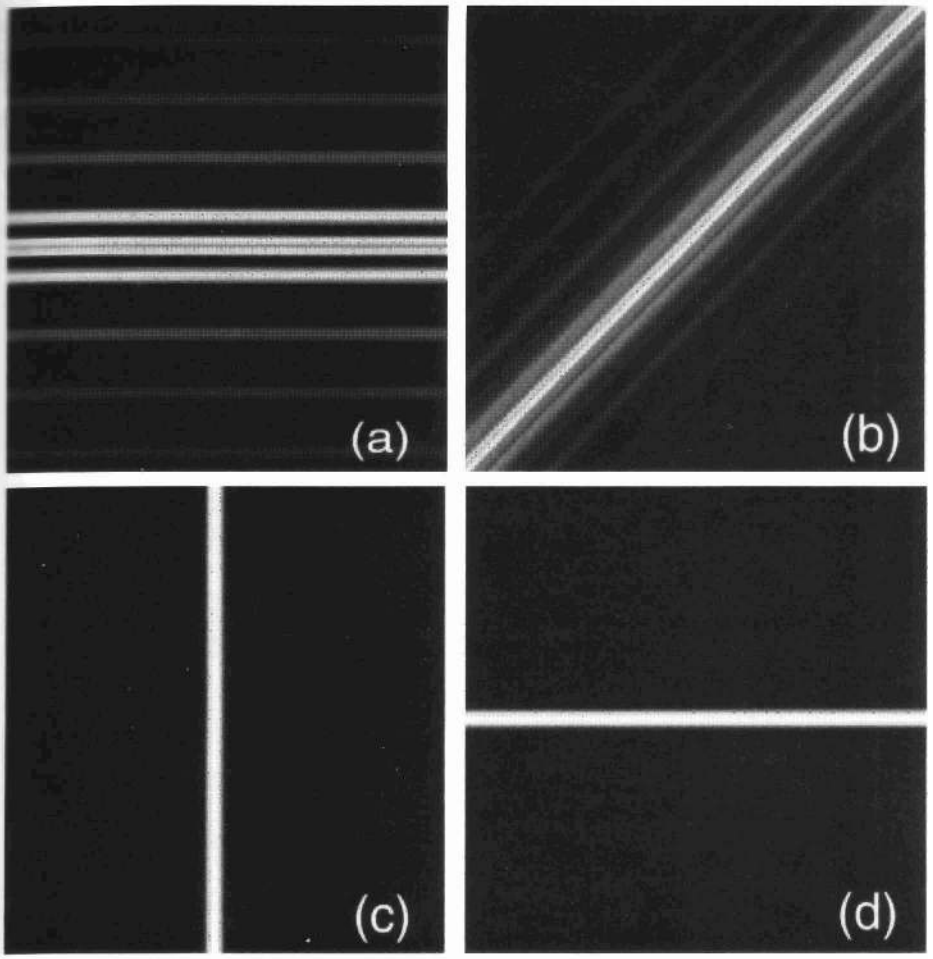

FIG. 10. Simulated echo-planar and spiral images: average velocity of 40 cm/s. (a)–(c) Echo-planar images for horizontal, diagonal, and vertical vessel orientations, respectively. (d) Spiral image.

The disparity in these images stems from the fundamental differences in the *k*-space trajectories of these sequences. With echo-planar imaging, the discontinuous behavior of k_u accounts for the ghosting artifacts when a component of flow exists in the readout direction. The flow compensation in the blip direction leads to no apparent artifacts when the vessel is vertically oriented. Although the impulse response for vertical flow is a shift and blur in the y direction, these effects are not apparent given the continuous stream of flowing material. The vessel distortion apparent in the oblique-flow case resembles the oblique-flow displacement artifact in 2DFT images. In 2DFT, this displacement artifact arises because the y position is encoded at a different time than the x position. However, the situation is more complicated in echo-planar because while the *y* position is encoded at time *TE*, the *x* position is encoded at different times due to the train of readout lines per excitation. This property is manifested in the *k*-space trajectory by the different linear variation of k_u with k_x for different readout lines.

With spiral imaging, the flow immunity is attributable to the three properties of $k_u(k_x, k_y)$ and $k_v(k_x, k_y)$ that were noted earlier. First, as indicated by Fig. 7b, k_u and k_v are small near the *k*-space origin. Second, the first moment is smoothly varying over the k_xk_y plane. Third, circular symmetry exists in which the direction of the $[k_u\ k_v]$ vector is largely pointed away from the origin. Interestingly, these properties of the spiral sequence are similar to those of a 2D projection reconstruction (2DPR) sequence in which radial spokes are acquired in *k*-space. The 2DPR sequence has also been shown to exhibit reduced flow artifacts (15, 16). For the vessel model considered in the simulation, the third property accounts for why the raw data differs very little from that obtained assuming no flow. By pointing away from the origin, $[k_u\ k_v]$ tends to be parallel with the direction of flow. The result is that the impulse response is a blur primarily in the flow direction, a relatively benign effect because of the streaming nature of flow. Alternatively this effect can be appreciated by noting that a horizontal vessel, for example, carries flowing material with a u component of velocity. A horizontal vessel also possesses a Fourier transform with most of its energy along the k_y axis, perpendicular to the vessel orientation. For a spiral sequence however, the k_u component of the trajectory is small along the k_y axis (see Fig. 6a along the k_y axis). Hence there occurs minimal distortion of the object.

The echo-planar trajectory lacks the three properties listed above due to the square-wave readout waveform, which creates discontinuities in k_u over (k_x, k_y) space, and the asymmetric nature of the *x* and *y* gradient wave-

forms. As indicated earlier, the artifacts would be worse if the time shifting had not been assumed to smooth out the k_v variation in (k_x, k_y) space. They would also be worse if we assumed physically realizable gradient waveforms instead of waveforms with arbitrarily fast rise times. On the other hand, the artifacts may become tolerable given moderate flow velocities, improved gradient strength, and appropriate orientation of the gradients with respect to the main flow direction. Moreover the simulations assumed image parameters that are more stringent than in usual implementations. Lowering the spatial resolution will alleviate flow effects by reducing the readout duration since the gradient first moments have a quadratic dependence on time. In addition, employing more interleaves and correspondingly fewer lines per acquisition will reduce the number of ghosts.

It should be emphasized that this comparison dealt with the relatively simple model of parabolic flow through a straight vessel. Although this basic model serves as an important reference, consideration of more complicated flow and geometries will also be significant in the assessment of these imaging sequences. For example, echo-planar showed good performance in this simulation when the vessel was oriented in the blip (y) direction, given the flow compensation in that direction. However, for more complex flow in the y direction, the phase induced by the relatively long flow-compensation gradients will likely take on greater significance. Therefore, a viable alternative is a partial-Fourier echo-planar acquisition (in k_y). Although a partial-Fourier sequence would continue to exhibit discontinuities and asymmetry in its velocity k-space trajectory, the sequence possesses a shorter TE and likely reduces the effects from higher-order motion because of the shorter gradient interval.

In summary, the velocity k-space formalism directly relates to the data acquisition, allowing for convenient simulation and analysis of flow experiments. Examination of the velocity k-space trajectories of echo-planar and spiral reveals fundamental differences that account for the substantially different flow-imaging performance. Although the focus of this paper has been on echo-planar and spiral, the formalism is general and should prove useful in analyzing other sequences. Possible future studies and extensions include the study of other k-space trajectories, pulsatility, higher-order flow, and more complex geometries.

REFERENCES

1. A. P. Crawley, M. S. Cohen, E. K. Yucel, B. Poncelet, T Brady, Single-shot magnetic resonance imaging: applications to angiography. *Cardiovasc. Int. Radiol.* **15,** 32–. (1992).
2. C. H. Meyer, B. S. Hu, D. G. Nishimura, A. Macovski, Fa spiral coronary artery imaging. *Magn. Reson. Med.* **28,** 202–213 (1992).
3. S. Duewell, C. P. Davis, G. McKinnon, B. Marincek, G. K Schulthess, Three- and four-dimensional mr angiograph with interleaved gradient-echo echo-planar sequences. "Proc., SMRM, 12th Annual Meeting, New York, 1993," p 385.
4. J. L. Duerk, O. P. Simonetti, Theoretical aspects of motion sensitivity and compensation in echo-planar imaging. *Magn. Reson. Imaging.* **1,** 643–650 (1991).
5. K. Butts, S. J. Riederer, Analysis of flow effects in echo-planar imaging. *J. Magn. Reson. Imaging.* **2,** 285–293 (1992).
6. P. Irarrazabal, D. Nishimura, Quantification and comparison of flow distortion for fast imaging, *in* "Proc., SMRM, 12th Annual Meeting, New York, 1993," p. 1257.
7. S. Ljunggren, A simple graphical representation of fourier-based imaging methods. *J. Magn. Reson.* **54,** 338–343 (1983).
8. D. B. Twieg, J. Katz, R. M. Peshock, A general treatment of NMR imaging with chemical shifts and motion. *Magn. Reson. Med.* **5,** 32–46 (1987).
9. J. S. Petersson, J.-O. Christoffersson, K. Golman, MRI simulation using the k-space formalism. *Magn. Reson. Imaging* **11,** 557–568 (1993).
10. D. N. Firmin, R. H. Klipstein, G. L. Hounsfield, M. P. Paley, D. B. Longmore, Echo-planar high-resolution flow velocity mapping. *Magn. Reson. Med.* **12,** 316–327 (1989).
11. R. M. Weisskoff, A. P. Chawley, V. Wedeen, Flow sensitivity and flow compensation in instant imaging, *in* "Proc., SMRM, 9th Annual Meeting, New York, 1992," p. 398.
12. Z. H. Cho, C. B. Ahn, Phase error corrected interlaced echo planar imaging, *in* "Proc., SMRM, 6th Annual Meeting, New York, 1987," p. 912.
13. F. Farzaneh, S. J. Riederer, Hybrid imaging with gradient-recalled sliding echos, *in* "Proc., SMRI, 7th Annual Meeting, Los Angeles, 1989," p. 70.
14. O. P. Simonetti, P. Wielopolski, J. L. Duerk, Experimental evaluation of flow effects in echo-planar imaging, *in* "Proc., SMR, 2nd Meeting, San Francisco, 1994," p. 460.
15. D. G. Nishimura, J. I. Jackson, J. M. Pauly, On the nature and reduction of the displacement artifact in flow images. *Magn. Reson. Med.* **22,** 481–492 (1991).
16. C. H. Glover, J. M. Pauly, Projection reconstruction techniques for reduction of motion effects in MRI. *Magn. Reson. Med.* **28,** 275–289 (1992).